Journal of Materials Chemistry

Cite this: J. Mater. Chem., 2012, 22, 9645

www.rsc.org/materials

PAPER

Fabrication of superior-performance SnO_2@C composites for lithium-ion anodes using tubular mesoporous carbon with thin carbon walls and high pore volume†

Fei Han,[a] Wen-Cui Li,[a] Ming-Run Li[b] and An-Hui Lu*[a]

Received 5th March 2012, Accepted 15th March 2012
DOI: 10.1039/c2jm31359f

A tubular composite, including ultrafine SnO_2 particles encapsulated in ordered tubular mesoporous carbon with thin walls and high pore volume, is fabricated through the *in situ* hydrolysis method. It is observed that up to 80 wt% of SnO_2 particles with size between 4–5 nm are highly dispersed and homogeneously encapsulated in the mesopore channels and no bulky aggregates are visible. The tubular composite exhibits a considerably high reversible capacity of 978 mA h g^{-1} and a high initial efficiency of 71% at a current density of 200 mA g^{-1} between 0.005–3 V. Its reversible capacity even increases up to 1039 mA h g^{-1} after 100 cycles, which is much higher than the conventional theoretical capacity of SnO_2 (782 mA h g^{-1}), meanwhile, it also displays fast discharge/charge kinetics at a high current density of 1500 mA g^{-1}. The excellent electrochemical performance is ascribed to its unique mesostructure by recruiting tubular mesoporous carbon with thin carbon walls (~2 nm) and high pore volume (2.16 cm^3 g^{-1}). This tubular nanostructure provides confined nanospace for hosting immobilized ultrafine SnO_2 with high loading, compensates volume expansion of SnO_2, warrants efficient contact between nanoparticles and carbon matrix before and after Li^+ insertion. We believe this special structure model might be extended for the fabrication of other cathode and anode electrode materials, to achieve high performance LIBs.

1. Introduction

Owing to the capacity and safety concerns with respect to pure Li metal, carbon-based materials have received considerable attention as anodes in Li-ion batteries (LIBs).[1] To date, graphite is still the most commonly used anode material. The lithium storage capacity of graphite is limited to 372 mA h g^{-1}, which greatly restricts the development of LIBs with high energy density. Thus, it is extremely necessary to explore new carbon materials to enhance the storage capacity, durability and rate performance. In the past decade, substantial efforts have been made to satisfy these requirements. Among them, many novel carbon materials including carbon nanotubes,[2] graphene sheets,[3] and amorphous carbon[1c,4] have been investigated with the aim of a replacement for graphite. However, carbon materials simultaneously possessing both a high reversible capacity >600 mA h g^{-1} and an initial coulombic efficiency >60% have not yet been reported.

To overcome the limitations of carbon materials, introduction of other compounds (such as Sn,[5a] Si,[5b,5c] SnO_2,[5d] and Co_3O_4[5e]) into the carbon is considered to be a promising strategy for the preparation of high-performance LIBs. SnO_2 has been extensively investigated as a novel anode material for LIBs, owing to its high theoretical reversible capacity (~782 mA h g^{-1}), moderate operating voltage, and good rate performance.[6] Unfortunately, the practical application of pure SnO_2 anode in LIBs is hampered by a low initial coulombic efficiency because of the irreversible reaction in the first cycle and poor material cycle stability arising from the large specific volume expansion (~250 vol%) during the discharge/charge processes, thus leading to pulverization and consequent loss of electrical contact with the current collector and an increase of electrical resistance between particles.[7] Meanwhile, it has been confirmed that the small and active Sn particles derived from the reaction of SnO_2 and Li^+ tend to aggregate into larger and inactive Sn clusters during cycling.[8] This also results in a deterioration of the reversible capacity. To overcome these obstacles, fabrication of carbon supported SnO_2 composites is considered to be an effective strategy to improve the electrochemical performance, which integrates the advantages of carbon and SnO_2 materials.[5d,9]

[a]State Key Laboratory of Fine Chemicals, School of Chemical Engineering, Faculty of Chemical, Environmental and Biological Science and Technology, Dalian University of Technology, Dalian 116024, P. R. China. E-mail: anhuilu@dlut.edu.cn
[b]State Key Laboratory of Catalysis, Dalian Institute of Chemical Physics, Chinese Academy of Sciences, Dalian 116023, P. R. China

† Electronic supplementary information (ESI) available. See DOI: 10.1039/c2jm31359f

Spherical core–shell SnO_2@C nanostructures were proposed with the idea of utilization of the free cavity for the compensation of the volume expansion of SnO_2 and carbon shell to improve the electrical conductivity.[9b,10] It is possible however that the spherical structures may display an inferior electrical conductivity due to the small contact area between adjacent spheres, and insufficient contact between the core and the shell during cycles (Scheme S1†). The encapsulation of SnO_2 nanoparticles (NPs) into carbon nanotubes[9a,11a] or dispersion of SnO_2 NPs on graphene sheets[9c,11b] were found to be beneficial for improving the rate capability, where the carbon matrix acted as an effective electron transfer medium. However, these composites suffered from a remarkable aggregation of SnO_2 NPs during cycles.[11c,11d] In addition, the stiff carbon walls of the carbon nanotubes are not suitable for buffering the huge volume expansion.[11e] These previous studies demonstrate that the selection of a carbon matrix is of crucial importance for improving the performance of SnO_2@C anodes. Moreover, Qiao *et al.* have reported the rod-type ordered mesoporous carbon (CMK-3) encapsulated SnO_2 composite as anode of LIBs.[12a] The loading of SnO_2 was only 17 wt% because of the low pore volume and thick pore walls of CMK-3 as well as their hydrophobic nature. The initial coulombic efficiency presented about 36% and the reversible capacity was 546 mA h g^{-1} after 35 cycles.[12a] Sun *et al.* have enhanced the loading of SnO_2 up to 72 wt% using ordered bimodal mesoporous carbon as a matrix, whereas the initial coulombic efficiency only reached 46% and the reversible capacity was 396 mA h g^{-1} after 50 cycles.[12b] The electrochemical performance of SnO_2@ordered mesoporous carbon composites should be further improved to satisfy the practical application.

Inspired by the aforementioned studies, we predicted that an ideal carbon matrix should have the following features: open pore channels with optimal size not only allowing easy impregnation SnO_2 precursor and ion transportation, but also providing a confined environment for the immobilization of SnO_2 NPs; a large pore volume for hosting a high amount of SnO_2 and allowing volume expansion during Li^+ insertion/extraction; and high surface area for good contact between SnO_2 NPs and the carbon matrix. In order to further improve the electrochemical performance of SnO_2-based anodes, we select CMK-5 as a matrix, which possesses tubular mesopore channels, thin carbon walls, and high pore volume,[13] have fabricated such tubular composite through the *in situ* hydrolysis method with a high loading of SnO_2 up to ~80 wt% and immobilized ultrafine SnO_2 NPs with sizes between 4–5 nm. This composite has been named SnO_2-80@CMK-5, which, as an anode material, exhibits a high initial efficiency of 71% and a considerably high reversible capacity of 978 mA h g^{-1} at a current density of 200 mA g^{-1}. Its reversible capacity even increases up to 1039 mA h g^{-1} after 100 cycles, which is much higher than the conventional theoretical capacity of SnO_2. As far as we know, this value is highest among those so far reported for the SnO_2 and carbon composite anodes. Remarkably, the SnO_2-80@CMK-5 anode also exhibits fast discharge/charge kinetics at a high current density of 1500 mA g^{-1}, suggesting the outstanding rate capability. Moreover, the thin carbon walls (~2 nm) have a good flexibility to effectively accommodate the strain of volume change of SnO_2 NPs, prevent particles aggregation and improve safety.[11e,14] It can be noted that the electrochemical performance of SnO_2-80@CMK-5 tubular composite is evidently better than the previous tin-based NPs@ordered mesoporous carbon composites.[12,15]

2. Experimental

Materials and syntheses

The preparation of mesoporous carbon, CMK-3 and CMK-5, has been described previously.[13c,16a,16b] A typical synthesis of SnO_2@CMK-5 composites was as follows:[16c] $SnCl_4 \cdot 5H_2O$ (1 g, 99 wt%) was dissolved in 1 mL of deionized water. 0.6 mL of this solution was added into 0.2 g CMK-5 under stirring at 25 °C. After all the solution had been absorbed, the powder was put into a Teflon bottle containing 14 wt% ammonia solution (4 mL), without direct contact to the ammonia solution. After sealing, the bottle was heated in an oven at 90 °C for 3 h to hydrolyze the tin precursor *in situ*. The product was then washed several times with deionized water and ethanol, and dried at 90 °C. The impregnation and conversion steps were repeated several times in order to increase the SnO_2 loading. Finally, the composite was heated to 300 °C for 1 h, and 550 °C for 3 h in an argon atmosphere, with a heating rate of 2 °C min^{-1}. Samples were denoted SnO_2-80@CMK-5 and SnO_2-60@CMK-5 for the different SnO_2 loadings as measured by a TG analyses. Nanocast SnO_2 was prepared by calcination of SnO_2-80@CMK-5 at 550 °C in air. For the synthesis of the SnO_2-60@CMK-3 composite, a similar procedure was used, only this time using CMK-3 as the matrix.

Characterization

Thermogravimetric analysis was measured from room temperature to 800 °C in air with a heating rate of 10 °C min^{-1} using a STA449 F3 Jupiter thermogravimetric analyzer (NETZSCH). The X-ray diffraction (XRD) measurements were taken on a Rigaku D/Max 2400 diffractometer using Cu-Kα radiation (40 kV, 100 mA, $\lambda = 1.5406$ Å). Transmission electron microscopy (TEM) images were obtained with a FEI Technai F30 or a Hitachi HF2000 transmission electron microscope, equipped with a cold field emission gun. In order to better observe the dispersion and sizes of the SnO_2 NPs, samples were embedded in Spurr's resin and cut into 60 nm thin sections using a microtome. Surface area and porosity were determined by N_2 adsorption at 77 K with a Micromeritcs Tristar 3000 analyzer.

Electrochemical characterization

Electrochemical experiments were performed *via* CR2025 coin-type test cells assembled in an argon-filled glove box with lithium metal as the counter and reference electrodes at room temperature. For preparing working electrodes, a mixture of active material (SnO_2@C or Nanocast SnO_2), conductive carbon black and commercial LA133 (water-based binder, Indigo, China, Essential Component: PAN) in water at a weight ratio of 80 : 10 : 10 was pasted on rough Cu foil with Celgard 2400 membrane as the separator to isolate electrons. CMK-5 anode was prepared by mixing 80 wt% CMK-5, 5 wt% conductive carbon black, and 15 wt% LA133 as the binder. The electrolyte consists of a solution of 1M $LiPF_6$ in dimethyl carbonate (DMC), ethyl methyl carbonate (EMC) and ethylene carbonate (EC) (1 : 1 : 1 v/v/v) with 2 wt% fluorinated ethylene carbonate (FEC)

as an additive. The discharge/charge measurements were carried out at different current densities on a Land CT2001A battery test system. The specific capacity of the SnO_2@C composites was calculated by using the total mass of SnO_2 and carbon. Cyclic voltammogram (CV) measurements and electrochemical impedance spectra (EIS) were performed on CHI660D electrochemical workstation. After 100 cycles, all cells were disassembled and washed in DMC to remove the residue in an argon-filled glove box.

3. Results and discussion

The synthesis procedure of such a SnO_2@CMK-5 composite is illustrated in Fig. 1. In order to highlight the advantages of CMK-5 which possesses tubular mesopore channels, thin carbon walls, and high pore volume, another mesoporous carbon CMK-3 with thick pore walls (~7 nm) was employed as a control. CMK-5 and CMK-3 were synthesized using SBA-15 as a template according to previous reports.[13d,16a,16b] $SnCl_4 \cdot 5H_2O$ solution was impregnated into the mesopore channels of the carbon matrixes, and then converted to $Sn(OH)_4$ after ammonia treatment. A subsequent thermal treatment at 550 °C for 3 h in an argon atmosphere led to the formation of SnO_2@CMK-5 and SnO_2@CMK-3 composites. As the reversible capacity of these composites depends on the SnO_2 content, a high loading of SnO_2 was achieved by repeating the impregnation and ammonia treatment.

To quantify the SnO_2 loading of the SnO_2@C composites, a TG technique was used under air. As shown in Fig. 2a, the mass loss below 600 °C is attributed to the combustion of carbon. At 800 °C, the SnO_2 content is *ca.* 60 wt%. XRD was used to characterize the crystallographic structures. In Fig. 2b, all the reflections can be indexed to tetragonal rutile-like SnO_2 (JCPDS; No. 41-1445), with no other phases detected. All peaks particularly the main characteristic diffractions at (110), (101), (200), and (211) are broad, indicating the existence of an extremely fine nanocrystalline material. Based on the Scherrer formula, the estimated sizes of the SnO_2 NPs in CMK-3 and CMK-5 are *ca.* 4.1 and 4.3 nm (Table 1) respectively. Such ultrafine SnO_2 NPs are formed owing to a restrictive effect of the small mesopores in carbon matrix.

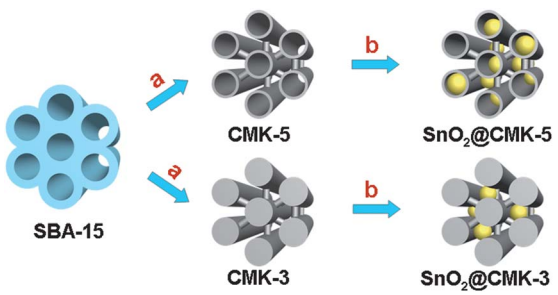

Fig. 1 Illustration of the synthesis principles of ultrafine SnO_2 NPs immobilized in the mesopore channels of mesoporous carbon. a: Impregnation with carbon precursors, followed by polymerization, carbonization, and leaching of SBA-15; b: Impregnation with $SnCl_4 \cdot 5H_2O$ aqueous solution, ammonia treatment, and thermal annealing.

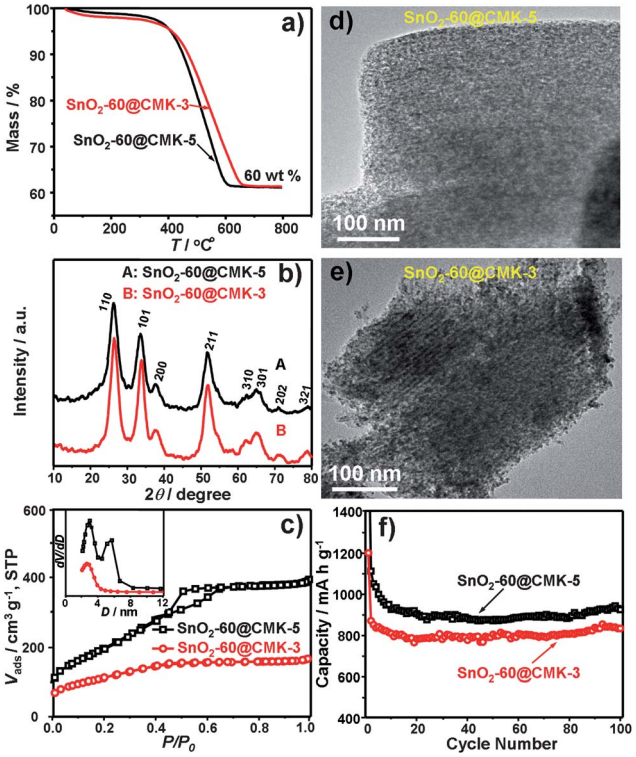

Fig. 2 a) TG curves, b) wide-angle XRD patterns and c) N_2 sorption isotherms and inset pore size distribution curves, d) and e) TEM images of composites based on different matrices, and f) cycle performance of composites. Test conditions: current density of 200 mA g^{-1} between 0.005 and 3 V, by taking the carbon mass of SnO_2@C into account.

The porous features of the SnO_2@C composites were determined using N_2 adsorption technique at 77 K. As seen in Fig. 2c, the N_2 sorption isotherms of the SnO_2@C composites are of type-IV, indicating mesoporous characteristics. The pore size distributions (Fig. 2c inset) show that SnO_2-60@CMK-5 has a bimodal pore system concentrated at 2.6 and 5.0 nm; whereas, SnO_2-60@CMK-3 has a monomodal mesopore distribution concentrated at 2.6 nm. The calculated textural parameters of these samples are summarized in Table 1. The product SnO_2-60@CMK-5 has a higher BET surface area (726 m^2 g^{-1}) and larger total pore volume (0.69 cm^3 g^{-1}) than that (405 m^2 g^{-1} and 0.22 cm^3 g^{-1}) of the SnO_2-60@CMK-3. Based on the pore parameters of the parent carbon, the filling degrees of the mesopores are calculated to be ~10 vol% for SnO_2-60@CMK-5 and ~23 vol% for SnO_2-60@CMK-3 (for details, see the ESI†).

The TEM images of SnO_2-60@CMK-5 and SnO_2-60@CMK-3 (Fig. 2d, e and Fig. S2†) show that these composites retain the same mesostructure and morphology as the carbon matrix. By looking at the external surface of the SnO_2-60@CMK-5 composite, almost no SnO_2 NPs are observed, indicating a perfect encapsulation of the SnO_2 NPs in the CMK-5 matrix. Clearly, SnO_2 NPs are highly dispersed and homogeneously encapsulated in the mesopore channels with a uniform size of 4–5 nm, and no bulky aggregates are visible. The particle sizes of SnO_2 are similar to that of the mesopores, indicating a confined effect in the mesopore channels. A similar confined effect has previously been reported by us with γ-Fe_2O_3 fully encapsulated

Table 1 Textural parameters of mesoporous carbon, SnO_2@C composites, and Nanocast SnO_2[a]

Sample	S_{BET} (m^2 g^{-1})	V_{total} (cm^3 g^{-1})	D_{peak} (nm)	D_{size} (nm)
CMK-3[b]	1042	0.92	3.7	—
CMK-5[b]	1770	2.16	3.0, 5.5	—
SnO_2-60@CMK-3	405	0.22	2.6	4.1
SnO_2-60@CMK-5	726	0.69	2.6, 5.0	4.3
SnO_2-80@CMK-5	383	0.18	—	4.9
Nanocast SnO_2	54	0.21	2.6, 15	8.2

[a] S_{BET}: BET specific surface area was calculated over the P/P_0 range 0.03 to 0.25; V_{total}: total pore volume at $P/P_0 = \sim 0.99$; D_{peak}: pore sizes at the maximum of the pore size distributions calculated based on the adsorption branch using BJH method; D_{size}: crystallite sizes were calculated by the Scherrer formula. [b] N_2 sorption isotherms and inset pore size distribution curves in Fig. S1.†

in the channels of CMK-5.[13d] This strongly indicates that the unique thin wall structure makes this particular carbon an ideal matrix for the encapsulation of metal oxide NPs. In contrast, the TEM image of SnO_2-60@CMK-3 shows that SnO_2 NPs have not been fully encapsulated in the mesopores of the CMK-3. A small amount of SnO_2 NPs emerge on the external surface of the carbon matrix, suggesting that CMK-3 does not have the capability to fully encapsulate of 60 wt% of SnO_2.

The electrochemical performances of these two composites were conducted at a current density of 200 mA g^{-1} over a voltage range of 0.005–3 V (Fig. 2f). The SnO_2-60@CMK-5 shows a high Li^+ storage capacity and high discharge capacity 917 mA h g^{-1} (based on the total mass of SnO_2@C), after 100 cycles. In contrast, the SnO_2-60@CMK-3 anode shows a relatively low value of 825 mA h g^{-1}. For comparison, the cycle performance of sample SnO_2-60@C/SBA-15 including a small pore channel (3 nm) without encapsulating SnO_2 nanoparticles is also tested. This experiment confirmed that CMK-5 is the most suitable matrix for the preparation of SnO_2@C composite anode (Fig. S3†). The high performance of the SnO_2-60@CMK-5 composite is attributed to the unique properties of CMK-5, *i.e.*, large capability for complete encapsulation of SnO_2 NPs, and the SnO_2 NPs in the CMK-5 matrix are more effectively immobilized and utilized than those in CMK-3. Thus CMK-5 has been selected as the host for all subsequent studies. This has the aim of maximizing the loading of SnO_2 and ensuring an adequate void space for volume expansion of SnO_2 and helping with ion transport. By assuming a simple configuration for the composite (see the ESI†), we calculated that when ~27 vol% of the total pore volume of SnO_2@CMK-5 was occupied by SnO_2 NPs, corresponding to 80 wt% SnO_2 loading after Li^+ insertion, the expanded SnO_2 would occupy 94 vol% of the total pore volume of the composite. This gives the maximum loading ensuring sufficient space for volume expansion of SnO_2. We thus prepared SnO_2-80@CMK-5 composite with 80 wt% SnO_2 loading.

As shown in Fig. 3a, the TG curves shows that a composite with 80 wt% SnO_2 can indeed be prepared. For comparison and to highlight the impact of the thin carbon walls, we prepared pure SnO_2 (named Nanocast SnO_2) *via* calcination of SnO_2-80@CMK-5 composite at 550 °C in air. The XRD patterns in Fig. 3b show that the Nanocast SnO_2 is similar to SnO_2-80@CMK-5 but with more intense and sharper peaks, indicating an increased particle size. The N_2 adsorption isotherms (Fig. 3c) of Nanocast SnO_2 show mesoporous features, with larger mesopore channels of ~15 nm, whereas SnO_2-80@CMK-5 is microporous. Of course, with an increase in the SnO_2 loading, the specific surface area and pore volume of the composites will decrease (Table 1). The TEM image in Fig. 3d shows that Nanocast SnO_2 has a larger average particle size of ~14 nm (Fig. S4†). The increase in particle size is ascribed to the growth of the unconfined crystals accompanied by deprotection of the thin carbon walls of CMK-5 during combustion.[17a] Nevertheless, as seen in Fig. 3e and Fig. S5,† a perfect hexagonal mesostructure of SnO_2-80@CMK-5 is clearly observed, and the energy dispersive X-ray spectroscopy (EDX) pattern (Fig. 3e, inset) confirms the presence of Sn, O, and C elements, suggesting that

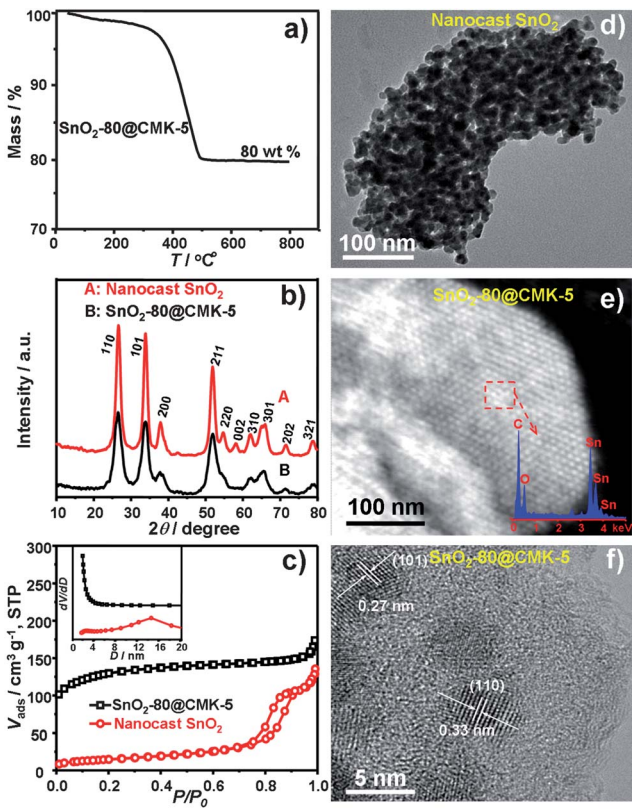

Fig. 3 a) TG curve of SnO_2-80@CMK-5; b) wide-angle XRD patterns, and c) N_2 sorption isotherms and pore size distributions (inset) of Nanocast SnO_2 and SnO_2-80@CMK-5; d) TEM image of Nanocast SnO_2, e) STEM (inset: EDX pattern) and f) HRTEM images of SnO_2-80@CMK-5.

SnO_2 NPs are highly dispersed within the carbon matrix. A high-resolution TEM image (Fig. 3f) shows that the SnO_2 NPs are fully encapsulated within the carbon framework, whose lattice fringes exist with *d* spacing values of 0.27 and 0.32 nm, corresponding to the (101) and (110) planes respectively of SnO_2. One can envisage that the close contact between SnO_2 NPs and thin carbon walls allows good electron transfer pathways. The particle size of SnO_2 NPs is *ca.* 5 nm, which is in good agreement with the size calculated based on the XRD patterns.

The discharge/charge performances of SnO_2-80@CMK-5 and Nanocast SnO_2 were evaluated at a current density of 200 mA g^{-1}. For comparison, pure CMK-5 was also tested under the same conditions. All results are compiled in Fig. 4a, together with the data of SnO_2-60@CMK-5. The capacity of Nanocast SnO_2 fades rapidly. This is ascribed to the pulverization of SnO_2 particles in the absence of carbon protection. CMK-5 is stable but has a low capacity. In sharp contrast, the SnO_2@CMK-5 composites exhibit improved cycle stability and a high reversible specific capacity. It is striking to note that SnO_2-80@CMK-5 displays a very high and stable reversible capacity of ~978 mA h g^{-1} in the initial 10 cycles, and 1039 mA h g^{-1} after 100 cycles. It is interesting to observe that the phenomena of the consistent enhancement in reversible capacity with the cycle number, which is well-documented for the nanostructured transition metal oxides in the literature,[11e,17b] but rarely been reported for SnO_2-based materials. We speculate that capacity increase is attributed to the reversible growth of a polymer gel-like film resulting from kinetically activated electrolyte degradation.[17c,17d] Another reason is that an activation step is required to electrochemically activate all SnO_2 nanoparticles in SnO_2-80@CMK-5 anode during cycles.[17e] This is due to the relatively lower surface area of SnO_2-80@CMK-5 than that of SnO_2-60@CMK-5, the electrolyte needs more time to permeate and contact with those deeply buried SnO_2 nanoparticles of the SnO_2-80@CMK-5 composite. To the best of our knowledge, this value is the highest among those so far reported for SnO_2@C electrodes. We have summarized (Table S1†) the literature data on electrochemical performance of SnO_2@C anodes for LIBs. In view of the contents of SnO_2 and CMK-5, using computational models (see the ESI†),[9c] a practical capacity of SnO_2 from the SnO_2@CMK-5 composite is calculated to be 1133 mA h g^{-1}, which is considerably higher than its theoretical value 782 mA h g^{-1}.[7a,7d,9b] How does this happen?

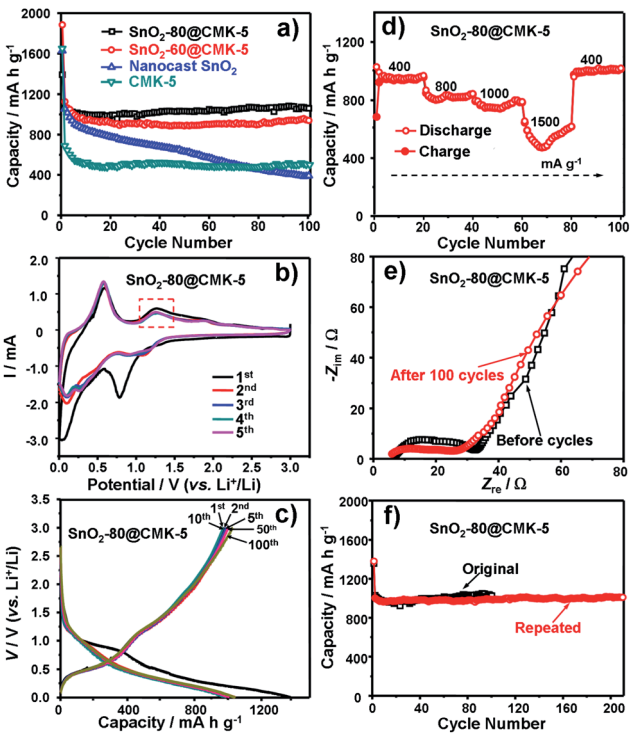

Fig. 4 a) Cycle performance of electrodes based on different SnO_2 content at a current density of 200 mA g^{-1} between 0.005 and 3 V, b) cyclic voltammograms, c) galvanostatic discharge/charge profiles, and d) rate performance, e) electrochemical impedance spectra of SnO_2-80@CMK-5 composite. f) Cycle performance of original and repeated SnO_2-80@CMK-5 sample (note: the repeated experiments were conducted by another independent operator following the same procedures, starting from the synthesis of CMK-5 and SnO_2-80@CMK-5 composite, till assembling and testing the cell.).

It is known that SnO_2@C electrodes react with electrolyte in the following processes:

$$Li^+ + e^- + \text{electrolyte} \rightarrow \text{SEI (Li)} \quad (1)$$

$$SnO_2 + 4Li + 4e^- \rightarrow Sn + 2Li_2O \quad (2)$$

$$Sn + xLi^+ + xe^- \leftrightarrow Li_xSn\ (x \leq 4.4) \quad (3)$$

$$C_6 + yLi^+ + ye^- \leftrightarrow Li_yC_6\ (y \leq 4.4) \quad (4)$$

The conventional theoretical capacity of SnO_2 (782 mA h g^{-1}) is calculated based on the reversible reaction (3), while reaction (2) is briefly considered to be an irreversible process. This is because the Li_2O matrix acts as a buffer zone and prevents the nanoparticles aggregating, but Li_2O is regarded as an electrochemically inactive material for LIBs.[18a] Recent works have indicated that reaction (2) for most metal compounds is reversible in view of the thermodynamics.[17e,18a–c] The reversibility of reaction (2) is mainly influenced by the intrinsic conductivity of SnO_2, grain size of LiO_2 and Sn, their degree of dispersion and the contact degree with conductive additives. For as-prepared SnO_2@CMK-5 tubular nanostructures, the SnO_2 highly dispersed in CMK-5 matrix have a fine particle size (<5 nm) and multiple electrical contacts directly with the carbon walls, even the contact area increases immensely after lithium insertion (Scheme S1†). These all make the electrochemically reactivity towards the formation/decomposition of Li_2O possible. If reaction (2) is reversible completely, the theoretical capacity of SnO_2 would increase up to 1494 mA h g^{-1}.[18d] Hence, we believe that reaction (2) is at least partially reversible in our case (6.4 Li per SnO_2 based on 1133 mA h g^{-1}), which contributes to the ultra-high reversible capacity.

To better demonstrate this conjecture, the cyclic voltammograms (CV) of SnO_2-80@CMK-5 at a scan rate of 0.2 mV s^{-1} were tested and the CV curves are displayed in Fig. 4b. As observed, the CV curves almost overlap from the second to fifth cycles, indicating that the cycle performance is considerably stable.[19] The difference between the first and latter cycles is partly ascribed to formation of the solid electrolyte interface (SEI) layer.[9e,20] Two reduction peaks at 0.8 and 0.05 V are observed

during the first cathodic scan. The former peak at 0.8 V, which is absent in the pure CMK-5 anode (Fig. S6†), is ascribed to the formation of an SEI layer and the reduction of SnO_2 to Sn. The latter peak is known to arise from the formation of Li_xSn alloys.[9b,9e,20] However, the oxidation peaks appearing at 0.6 and 1.25 V are correspondingly attributed to the de-alloying reaction, and the oxidation of Sn to SnO_2. The latter oxidation peak (1.25 V) is rarely seen in literature.[9b,9e,21] This strongly implies that the inverse process with Li_2O transition back to the Li^+ takes place in the current case.

Fig. 4c shows voltage profiles of the SnO_2-80@CMK-5 composite after 100 cycles. It can be seen that the first discharge and charge capacities are 1374 and 976 mA h g^{-1}, respectively. Surprisingly, the initial coulombic efficiency is high at 71%. Following the first cycle, the coulombic efficiency remains high (>98.5%) and is stable throughout the entire cycle tests, indicating that the formed surface SEI film retained intact and good reversibility of the electrochemical reactions. In addition, it is well-known that when the upper cutoff voltage of tin-based oxides is higher than 1.3 V, the Li_2O matrix will be destroyed, thus further the capacity fading is very drastic.[22a] In this study, The cycle performance over a voltage range of 0.005–3 V still is extremely stable, confirming the superiority of the structure stability of such tubular composite material.

Importantly, such a SnO_2-80@CMK-5 composite electrode allows discharge/charge at higher current densities (Fig. 4d). It delivers a rate capacity of *ca.* 950 mA h g^{-1} when first cycled at 400 mA g^{-1} for 20 cycles, 830 mA h g^{-1} at 800 mA g^{-1}, and 770 mA h g^{-1} at 1000 mA g^{-1}. Even at a high current density of 1500 mA g^{-1}, the specific capacity first declines rapidly but then increases to a value *ca.* 600 mA h g^{-1}. Moreover, when the current density returns to the initial 400 mA g^{-1} after 80 cycles, the composite electrode recovers its original capacity or even slightly higher (1004 mA h g^{-1} at the 100th cycle). The excellent rate performance of SnO_2-80@CMK-5 is undoubtedly due to its unique mesostructure, *i.e.*, thin carbon walls, abundant mesoporosity, ultrafine SnO_2 NPs, and good contact between SnO_2 NPs and carbon matrix (*i.e.* good electrical conductivity).

Furthermore, electrochemical impedance spectra measurements of SnO_2-80@CMK-5 before and after 100 cycles were also conducted (Fig. 4e) by applying a sine wave with amplitude of 5.0 mV over a frequency range 100 kHz–0.01 Hz. It can be seen that the cell impedance after 100 cycles is even lower than that of the cell before the cycle test, indicating that an "*in situ* activation" phenomenon occurs for the cell.[22b,22c] Such an improved performance is certainly attributed to the synergy between the carbon matrix and the SnO_2 NPs during cycles. Moreover, in order to test the reproducibility of our results, the same experimental procedure, starting from the preparation of CMK-5, SnO_2-80@CMK-5 and the cell, were independently repeated by another operator. As seen in Fig. 4f, the repeated experiment shows identical result as the original one (deviation < 4%), indicating a highly reproducible operation. The cycle performance of the repeated sample is also considerably stable and the reversible capacity retains 1022 mA h g^{-1} after 210 discharge/charge cycles.

Moreover, the spent SnO_2-80@CMK-5 was characterized by XRD and TEM after 100 cycles, respectively. The presence of metallic Sn was confirmed by XRD (Fig. S7†), indicating the reduction of SnO_2 to Sn during cycling, which is widely accepted to take place in SnO_2-based anodes.[6b,7c,21] The peaks of Sn with very low intensity indicate that the metallic NPs are rather small. From TEM and STEM observations (Fig. 5a, b and Fig. S8†), one can see that the ordered mesostructures remain intact and the Sn-based NPs are still homogeneously encapsulated within the carbon matrix before and after 100 cycles. No aggregated crystalline NPs are observed. This strongly indicates that such a unique carbon host effectively prevents the aggregation and/or pulverization of Sn-based NPs and stabilizes the cycle performance.[23] An EDX analysis of the chemical composition correlates well with the composite before cycles (Fig. 5b, inset).

The mechanism for such an excellent performance of SnO_2-80@CMK-5 composite as an anode is summarized below. The ultrafine SnO_2 NPs with average diameters of 4–5 nm offer a high reactive activity and shorten electronic and ionic transport lengths, leading to a superior capacity and excellent rate capability. Compared to the spherical core–shell structures described in the literature,[9b,10,18c] a large contact area between the carbon matrix (μm size grains in an elongated rod shape[13d]) as well as efficient contact area between SnO_2 NPs and the thin carbon walls enhances the electrical conductivity and suppresses the aggregation of SnO_2 NPs (Fig. 5c). The adequate void space of the mesopore channels can act as a "buffer zone" for accommodating volume expansion (~250 vol%) and prevent pulverization of SnO_2 NPs during discharge/charge processes. After Li^+ insertion, Sn-based NPs can expand along the mesochannels, increasing the contact areas between Sn-based NPs and carbon walls. In this way, the thin carbon walls can still act as mini-current collectors for the encapsulated SnO_2 NPs, and facilitate fast electron transport during the insertion/extraction processes (Fig. 5c). Combining the ultrahigh reversible capacity, high coulombic efficiency, stable cycle performance, and outstanding rate capability, we believe that such SnO_2@CMK-5 composites are promising superior candidates as anode materials in LIBs.

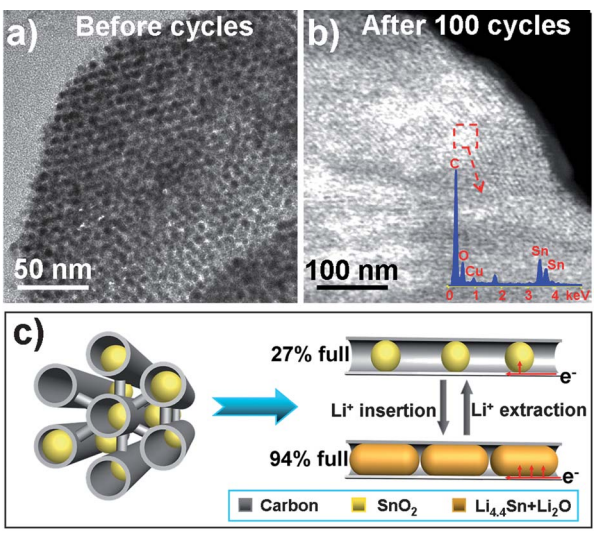

Fig. 5 TEM and STEM images of SnO_2-80@CMK-5 anode before (a) and after (b) 100 discharge/charge cycles at 200 mA g^{-1} (b inset: EDX pattern), c) schematic illustration of volume change during Li^+ insertion/extraction processes.

4. Conclusions

In summary, we have demonstrated that superior-performance Li-ion anodes can be fabricated using SnO_2@C composites with tubular mesoporous carbon having very thin carbon walls and large pore volume as the matrix. Up to 80 wt% of SnO_2 NPs with size between 4–5 nm can be fully encapsulated into the mesopore channels. This composite provides the suitable cushion space for the volume expansion of SnO_2 and warrants efficient contact pattern between SnO_2 NPs and carbon walls before and after Li^+ insertion. Such a composite anode integrates several advantages in one material: such as high reversible capacities (976 mA h g^{-1} of initial reversible capacity), excellent cycle performance (1039 mA h g^{-1} after 100 cycles), and superior rate performance (*ca.* 600 mA h g^{-1} at 1500 mA g^{-1}) for LIBs. Optimistically, this type of tubular mesoporous carbon could be extended for the fabrication of other cathode and anode electrode materials, to achieve high performance LIBs.

Acknowledgements

The project was supported by the Fundamental Research Funds for the Central Universities, the Program for New Century Excellent Talents in University of China and National Natural Science Foundation of China (NCET-08-0075, NECT-09-0254 and NSFC 21103184) and the PhD Programs Foundation (20100041110017) of Ministry of Education of China.

Notes and references

1 (*a*) G. Che, B. B. Lakshmi, E. R. Fisher and C. R. Martin, *Nature*, 1998, **393**, 346; (*b*) M. Winter, J. O. Besenhard, M. E. Spahr and P. Novák, *Adv. Mater.*, 1998, **10**, 725; (*c*) F. Bonino, S. Brutti, P. Reale, B. Scrosati, L. Gherghel, J. Wu and K. Müllen, *Adv. Mater.*, 2005, **17**, 743; (*d*) Y.-S. Hu, P. Adelhelm, B. M. Smarsly, S. Hore, M. Antonietti and J. Maier, *Adv. Funct. Mater.*, 2007, **17**, 1873; (*e*) T. Bhardwaj, A. Antic, B. Pavan, V. Barone and B. D. Fahlman, *J. Am. Chem. Soc.*, 2010, **132**, 12556.

2 (*a*) J. Zhang, Y.-S. Hu, J.-P. Tessonnier, G. Weinberg, J. Maier, R. Schlögl and D. S. Su, *Adv. Mater.*, 2008, **20**, 1450; (*b*) C. Masarapu, V. Subramanian, H. Zhu and B. Wei, *Adv. Funct. Mater.*, 2009, **19**, 1008.

3 (*a*) E. Yoo, J. Kim, E. Hosono, H. Zhou, T. Kudo and I. Honma, *Nano Lett.*, 2008, **8**, 2277; (*b*) S. Yang, X. Feng, L. Wang, K. Tang, J. Maier and K. Müllen, *Angew. Chem., Int. Ed.*, 2010, **49**, 4795.

4 (*a*) H. Zhou, S. Zhu, M. Hibino, I. Honma and M. Ichihara, *Adv. Mater.*, 2003, **15**, 2107; (*b*) B. Guo, X. Wang, P. F. Fulvio, M. Chi, S. M. Mahurin, X.-G. Sun and S. Dai, *Adv. Mater.*, 2011, **23**, 4661.

5 (*a*) D. Deng and J. Y. Lee, *Angew. Chem., Int. Ed.*, 2009, **48**, 1660; (*b*) C. K. Chan, H. L. Peng, G. Liu, K. Mcllwrath, X. F. Zhang, R. A. Huggins and Y. Cui, *Nat. Nanotechnol.*, 2008, **3**, 31; (*c*) H. Kim and J. Cho, *Nano Lett.*, 2008, **8**, 3688; (*d*) K. T. Lee, J. C. Lytle, N. S. Ergang, S. M. Oh and A. Stein, *Adv. Funct. Mater.*, 2005, **15**, 547; (*e*) S. Yang, X. Feng, S. Ivanovici and K. Müllen, *Angew. Chem., Int. Ed.*, 2010, **49**, 8408.

6 (*a*) Y. Idota, T. Kubota, A. Matsufuji, Y. Maekawa and T. Miyasaka, *Science*, 1997, **276**, 1395; (*b*) P. G. Bruce, B. Scrosati and J.-M. Tarascon, *Angew. Chem., Int. Ed.*, 2008, **47**, 2930.

7 (*a*) P. Meduri, C. Pendyala, V. Kumar, G. U. Sumanasekera and M. K. Sunkara, *Nano Lett.*, 2009, **9**, 612; (*b*) H. Li, Z. Wang, L. Chen and X. Huang, *Adv. Mater.*, 2009, **21**, 4593; (*c*) J. Y. Huang, L. Zhong, C. M. Wang, J. P. Sullivan, W. Xu, L. Q. Zhang, S. X. Mao, N. S. Hudak, X. H. Liu, A. Subramanian, H. Fan, L. Qi, A. Kushima and J. Li, *Science*, 2010, **330**, 1515; (*d*) C. Wang, Y. Zhou, M. Ge, X. Xu, Z. Zhang and J. Z. Jiang, *J. Am. Chem. Soc.*, 2010, **132**, 46; (*e*) H. Liu, X. Du, X. Xing, G. Wang and S. Z. Qiao, *Chem. Commun.*, 2012, **48**, 865.

8 I. A. Courtney, W. R. Mckinnon and J. R. Dahn, *J. Electrochem. Soc.*, 1999, **146**, 59.

9 (*a*) Y. Wang, H. C. Zeng and J. Y. Lee, *Adv. Mater.*, 2006, **18**, 645; (*b*) X. W. Lou, C. M. Li and L. A. Archer, *Adv. Mater.*, 2009, **21**, 2536; (*c*) S.-M. Paek, E. Yoo and I. Honma, *Nano Lett.*, 2009, **9**, 72; (*d*) J. Liu, W. Li and A. Manthiram, *Chem. Commun.*, 2010, **46**, 1437; (*e*) L. Ji, Z. Lin, B. Guo, A. J. Medford and X. Zhang, *Chem.–Eur. J.*, 2010, **16**, 11543; (*f*) W.-J. Cui, F. Li, H.-J. Liu, C.-X. Wang and Y.-Y. Xia, *J. Mater. Chem.*, 2009, **19**, 7202.

10 (*a*) Y.-G. Guo, J.-S. Hu and L.-J. Wan, *Adv. Mater.*, 2008, **20**, 2878; (*b*) X.-J. Wu and D. Xu, *Adv. Mater.*, 2010, **22**, 1516.

11 (*a*) C. Xu, J. Sun and L. Gao, *J. Phys. Chem. C*, 2009, **113**, 20509; (*b*) H. Wang, L.-F. Cui, Y. Yang, H. S. Casalongue, J. T. Robinson, Y. Liang, Y. Cui and H. Dai, *J. Am. Chem. Soc.*, 2010, **132**, 13978; (*c*) Y.-S. Hu, R. Demir-Cakan, M.-M. Titirici, J.-O. Müller, R. Schlögl, M. Antonietti and J. Maier, *Angew. Chem., Int. Ed.*, 2008, **47**, 1645; (*d*) H.-X. Zhang, C. Feng, Y.-C. Zhai, K.-L. Jiang, Q.-Q. Li and S.-S. Fan, *Adv. Mater.*, 2009, **21**, 2299; (*e*) G. Zhou, D.-W. Wang, F. Li, L. Zhang, N. Li, Z.-S. Wu, L. Wen, G. Q. Lu and H.-M. Cheng, *Chem. Mater.*, 2010, **22**, 5306.

12 (*a*) H. Qiao, J. Li, J. Fu, D. Kumar, Q. Wei, Y. Cai and F. Huang, *ACS Appl. Mater. Interfaces*, 2011, **3**, 3704; (*b*) G.-L. Xu, S.-R. Chen, J.-T. Li, F.-S. Ke, L. Huang and S.-G. Sun, *J. Electroanal. Chem.*, 2011, **656**, 185.

13 (*a*) S. H. Joo, S. J. Chol, I. Oh, J. Kwak, Z. Liu, O. Terasakl and R. Ryoo, *Nature*, 2001, **412**, 169; (*b*) S. Che, K. Lund, T. Tatsumi, S. Iijima, S. H. Joo, R. Ryoo and O. Terasaki, *Angew. Chem., Int. Ed.*, 2003, **42**, 2182; (*c*) A.-H. Lu, W.-C. Li, W. Schmidt, W. Kiefer and F. Schüth, *Carbon*, 2004, **42**, 2939; (*d*) A.-H. Lu, J.-J. Nitz, M. Comotti, C. Weidenthaler, K. Schlichte, C. W. Lehmann, O. Terasaki and F. Schüth, *J. Am. Chem. Soc.*, 2010, **132**, 14152.

14 (*a*) W.-M. Zhang, J.-S. Hu, Y.-G. Guo, S.-F. Zhong, W.-G. Song and L.-J. Wan, *Adv. Mater.*, 2008, **20**, 1160; (*b*) Y. Qiu, K. Yan and S. Yang, *Chem. Commun.*, 2010, **46**, 8359; (*c*) G. Wang, H. Liu, J. Liu, S. Qiao, G. M. Lu, P. Munroe and H. Ahn, *Adv. Mater.*, 2010, **22**, 4944.

15 (*a*) J. Fan, T. Wang, C. Yu, B. Tu, Z. Jiang and D. Zhao, *Adv. Mater.*, 2004, **16**, 1432; (*b*) I. Grigoriants, L. Sominski, H. Li, I. Ifargan, D. Autbach and A. Gedanken, *Chem. Commun.*, 2005, 921; (*c*) Y. Qiu, K. Yan and S. Yang, *Chem. Commun.*, 2010, **46**, 8359; (*d*) Z. Yu, S. Zhu, Y. Li, Q. Liu, C. Feng and D. Zhang, *Mater. Lett.*, 2011, **65**, 3072; (*e*) S. Ding, Z. Wang, S. Madhavi and X. W. Lou, *J. Mater. Chem.*, 2011, **21**, 13860.

16 (*a*) A.-H. Lu, W. Schmidt, B. Spliethoff and F. Schüth, *Adv. Mater.*, 2003, **15**, 1602; (*b*) A.-H. Lu, W. Schmidt, B. Spliethoff and F. Schüth, *Chem.–Eur. J.*, 2004, **10**, 6085; (*c*) Z. Wu, Q. Li, D. Feng, P. A. Webleyn and D. Zhao, *J. Am. Chem. Soc.*, 2010, **132**, 12042.

17 (*a*) R. W. J. Scott, N. Coombs and G. A. Ozin, *J. Mater. Chem.*, 2003, **13**, 969; (*b*) C. Ban, Z. Wu, D. T. Gillaspie, L. Chen, Y. Yan, J. L. Blackburn and A. C. Dillon, *Adv. Mater.*, 2010, **22**, E145; (*c*) S. Laruelle, S. Grugeon, P. Poizot, M. Dollé, L. Dupont and J.-M. Tarascon, *J. Electrochem. Soc.*, 2002, **149**, A627; (*d*) S. Grugeon, S. Laruelle, L. Dupont and J.-M. Tarascon, *Solid State Sci.*, 2003, **5**, 895; (*e*) L. Xiao, Y. Cao, J. Xiao, B. Schwenzer, M. H. Engelhard, L. V. Saraf, Z. Nie, G. J. Exarhos and J. Liu, *Adv. Mater.*, 2012, **24**, 1176.

18 (*a*) P. Polzot, S. Laruelle, S. Grugeon, L. Dupont and J.-M. Tatascon, *Nature*, 2000, **407**, 496; (*b*) X. Sun, J. Liu and Y. Li, *Chem. Mater.*, 2006, **18**, 3486; (*c*) X. W. Lou, J. S. Chen, P. Chen and L. A. Archer, *Chem. Mater.*, 2009, **21**, 2868; (*d*) J. Li, Y. Zhao, N. Wang and L. Guan, *Chem. Commun.*, 2011, **47**, 5238; (*e*) Y. Yu, C.-H. Chen and Y. Shi, *Adv. Mater.*, 2007, **19**, 993.

19 J. Ye, H. Zhang, R. Yang, X. Li and L. Qi, *Small*, 2010, **6**, 296.

20 Y. Yu, L. Gu, C. Wang, A. Dhanabalan, P. A. Aken and J. Maier, *Angew. Chem., Int. Ed.*, 2009, **48**, 6485.

21 Z. Wen, Q. Wang, Q. Zhang and J. Li, *Adv. Funct. Mater.*, 2007, **17**, 2772.

22 (*a*) Y. W. Xiao, J. Y. Lee, A. S. Yu and Z. L. Liu, *J. Electrochem. Soc.*, 1999, **146**, 3623; (*b*) S. Wang, J. Zhang and C. Chen, *J. Power Sources*, 2010, **195**, 5379; (*c*) C. Zhang, X. Peng, Z. Guo, C. Cai, Z. Chen, D. Wexler, S. Li and H. Liu, *Carbon*, 2012, **50**, 1897.

23 C. Kim, M. Noh, M. Choi, J. Cho and B. Park, *Chem. Mater.*, 2005, **17**, 3297.